7.3 Benchmark Channel: new physics from dijets

Editor(s): R. Harris
Contributor(s): N. Akchurin, S. Esen, K. Gumus, R. Harris

Inclusive dijet production ($pp \rightarrow 2\,\text{jets} + X$) is the dominant LHC process. Simple to observe, and rich in potential signals of new physics, dijets are expected to be one of the earliest CMS measurements. In this section we discuss the measured distributions and their systematic uncertainties. In section 17.4.2 and 17.4.3 we use these distributions to estimate our sensitivity to specific models of new physics.

7.3.1 Dijet Analysis

We use samples produced during Data Challenge 2004, generated using Pythia dijet processes mixed with pileup of minimum bias interactions for an assumed luminosity of 2×10^{33} cm^{-2} s^{-1}, simulated with OSCAR 2_4_5, and later reconstructed with ORCA 8_7_1. Jets are reconstructed as localized energy depositions in the CMS calorimeters arranged in a projective tower geometry. The jet energy E is defined as the scalar sum of the calorimeter tower energies inside a cone of radius $R = \sqrt{(\Delta\eta)^2 + (\Delta\phi)^2} = 0.5$, centered on the jet direction. The jet momentum $\vec{P}$ is the corresponding vector sum of energies, with the vector pointing in the tower direction. Both the jet energy and momentum are corrected back to the particles in the jet cone originating from the hard interaction excluding pileup [3]. We define the dijet system as the two jets with the highest p_{T} in an event (leading jets) and define the dijet mass $m = \sqrt{(E_1 + E_2)^2 - (\vec{P}_1 + \vec{P}_2)^2}$. We select events in which the leading jets each have $|\eta| < 1$. This cut enhances our sensitivity to new physics, produced at low $|\eta|$, compared to the predominantly t-channel processes from the QCD background. In all plots that are a function of dijet mass, we plot in bins of width equal to the Gaussian resolution measured in section 7.3.5.1.

7.3.2 Single Jet Triggers (MOVE ME TO TRIGGER CHAPTER)

In this section we propose the single jet trigger paths. We have been driven by the needs of the inclusive jet and dijet analysis. To measure jet spectra down to low jet E_T and dijet mass requires multiple triggers, of roughly equal total rate, and with appropriately chosen E_T thresholds and prescales. In figure 7.1 we show estimates of the L1 and HLT single jet trigger rates vs. corrected jet E_T. In table 7.4 we show the single jet trigger paths from L1 to HLT including thresholds, prescales and estimates of the rates. We find that the maximum allowed HLT rate is the constraining factor for trigering on jets. For luminosity scenario 1, 2 and 4 the highest E_T threshold at HLT was chosen to give a rate of roughly 2.5 Hz, as illustrated in figure 7.1, so that four triggers would saturate an allowed jet rate of roughly 10 Hz at HLT. The highest E_T threshold in each scenario is not prescaled. Lower thresholds are prescaled and are chosen at roughly half the E_T of the next highest threshold. This allows reasonable statistics in the overlap between the two samples, necessary for measuring trigger efficiencies and producing a continuous jet spectrum. Note that the total L1 jet rate required is only around 0.3 KHz, a small fraction of the L1 total bandwidth. Since we are limited by HLT, not L1, for each trigger path the L1 thresholds are chosen low enough to have a L1 trigger efficiency of more than 95% at the corresponding HLT threshold in the path, as

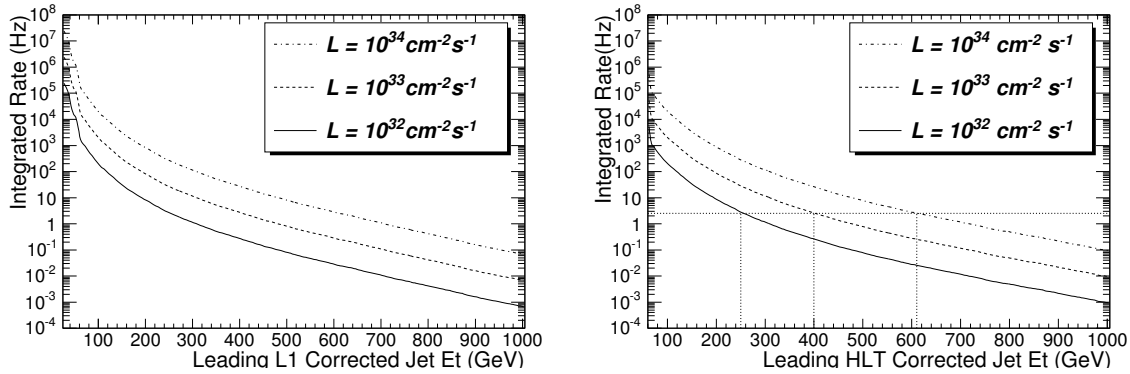

Figure 7.1: The integrated trigger rates at L1 (left) and HLT (right) above the E_T thresholds for the highest E_T jet is plotted versus the E_T threshold for three luminosity scenarios: $\mathcal{L} = 10^{32}\ \mathrm{cm}^{-2}\,\mathrm{s}^{-1}$ (solid) , and $\mathcal{L} = 10^{33}\ \mathrm{cm}^{-2}\,\mathrm{s}^{-1}$ (dashed), and $\mathcal{L} = 10^{34}\ \mathrm{cm}^{-2}\,\mathrm{s}^{-1}$ (dot-dashed). HLT thresholds that give 2.5 Hz are shown by vertical dotted lines.

shown in Figure 7.2. This strategy utilizes ten times more bandwidth at L1 than at HLT to insure that all of the resulting HLT sample has high enough trigger efficiency to be useful for analysis.

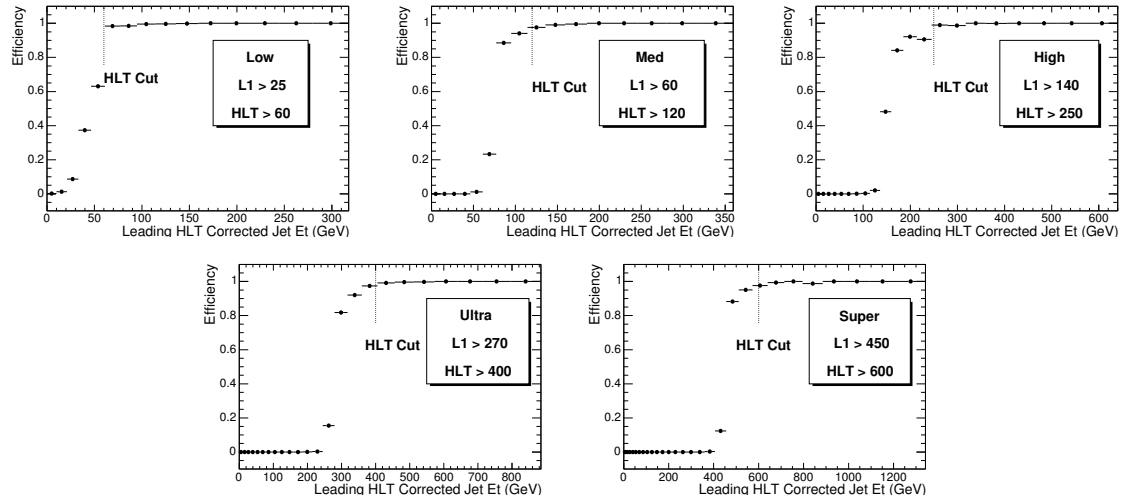

Figure 7.2: The efficiency for passing the L1 jet trigger is shown as a function of HLT corrected jet E_T for each of the trigger paths shown in table 7.4. The L1 thresholds were chosen to give an efficiency of greater than 95% at the corresponding HLT threshold.

Table 7.4 illustrates a trigger strategy to maintain the continuity of jet analysis as the luminosity increases over a time span of years. The most important feature is that each luminosity scenario maintains the thresholds introduced in the previous scenario, allowing combination of trigger samples over time. For the prescaled thresholds, we may increase the prescales, either in discrete steps or dynamically, to maintain the allowed HLT rate with increasing luminosity. However, to maintain maximum sensitivity to new physics, the highest E_T threshold must never be prescaled. For example, in table 7.4 when the luminosity increases by only a factor of 2 from Scenario 2 to Scenario 3, we double the prescales on the prescaled triggers

Path	L1				HLT	
	E_T Cut (GeV)	Unpres. Rate (KHz)	Prescale (N)	Presc. Rate (KHz)	E_T Cut GeV)	Rate (Hz)
Single Jet Triggers in Scenario 1: $\mathcal{L} = 10^{32}$ cm^{-2} s^{-1}						
High	140	0.034	1	0.044	250	2.8
Med	60	0.91	40	0.097	120	2.4
Low	25	3.9×10^1	2,000	0.146	60	2.8
Single Jet Triggers in Scenario 2: $\mathcal{L} = 10^{33}$ cm^{-2} s^{-1}						
Ultra	270	0.016	1	0.019	400	2.6
High	140	0.34	10	0.044	250	2.8
Med	60	9.1	400	0.097	120	2.4
Low	25	3.9×10^2	20,000	0.146	60	2.8
Single Jet Triggers in Scenario 3: $\mathcal{L} = 2 \times 10^{33}$ cm^{-2} s^{-1}						
Ultra	270	0.032	1	0.038	400	5.2
High	140	0.68	20	0.044	250	2.8
Med	60	18	800	0.097	120	2.4
Low	25	7.8×10^2	40,000	0.146	60	2.8
Single Jet Triggers in Scenario 4: $\mathcal{L} = 10^{34}$ cm^{-2} s^{-1}						
Super	450	0.013	1	0.014	600	2.8
Ultra	270	0.16	10	0.019	400	2.6
High	140	3.4	100	0.044	250	2.8
Med	60	9.1×10^1	4,000	0.097	120	2.4
Low	25	3.9×10^3	200,000	0.146	60	2.8

Table 7.4: Single jet trigger table showing path names, trigger thresholds in corrected E_T, prescales, and estimated rates at L1 and HLT for four different luminosity scenarios.

but don't change either the threshold or the prescale of the highest E_T trigger labelled Ultra. This allows us to maintain stability of the single jet trigger thresholds, and analyses that depend on them, with only modest increases in the total rate for single jets. When the HLT rate in the unprescaled trigger becomes intolerably high, a higher E_T threshold unprescaled trigger is introduced, and the old unprescaled trigger can then be prescaled as necessary.

To commission the calorimeters, or perform a one-time jet study, it may be desirable to have more jets. If we want to write more than roughly 10 Hz of single jets at HLT, we recommend using the thresholds in Table 7.4, but lowering the prescales to obtain more jets at low E_T. This is preferable to moving the threshold for the unprescaled trigger, or any of the triggers, and ending up with a special trigger that is only applicable for a given running period and difficult to combine with other samples.

7.3.3 Rates and Efficiencies from Jet Triggers

We use simulated data from the single jet triggers discussed in section 7.3.2. From the three trigger tables for luminosities of $L = 10^{32}$, 10^{33}, 10^{34} cm^{-2}s^{-1} we expect initial samples of size at least 100 pb^{-1}, 1 fb^{-1}, and 10 fb^{-1} respectively. This is from 10^6 seconds of collisions, equivalent to one month of continuous operation at 40% efficiency. In Fig. 7.3 we show

the rate expected from these triggers as a function of dijet mass. By construction there are

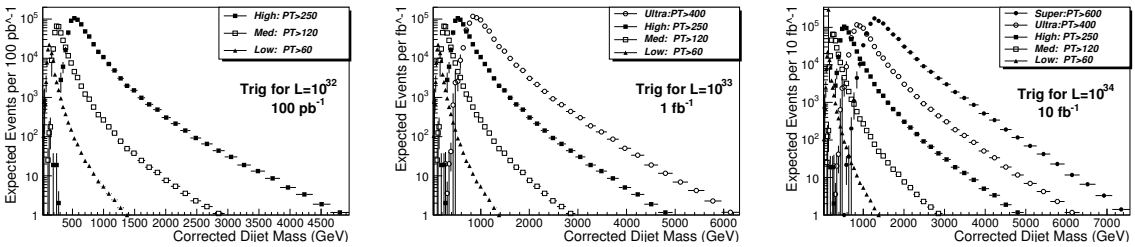

Figure 7.3: Rate of jet trigger as a function of dijet mass. The 3 plots correspond to 3 trigger tables, and each plot shows multiple triggers with various $p_{\rm T}$ thresholds and prescales.

comparable events in each trigger, and a high statistics overlap between triggers for a given table. We see that the highest mass dijet is expected to be 5, 6 and 7 TeV for samples of size 100 pb^{-1}, 1 fb^{-1}, and 10 fb^{-1} respectively. In Fig. 7.4 we show the trigger efficiency vs. dijet mass, measured for each trigger using the neighboring trigger with a lower $p_{\rm T}$ threshold, and explicitly show the mass cuts that are fully efficient. In Fig. 7.5 we show the data we

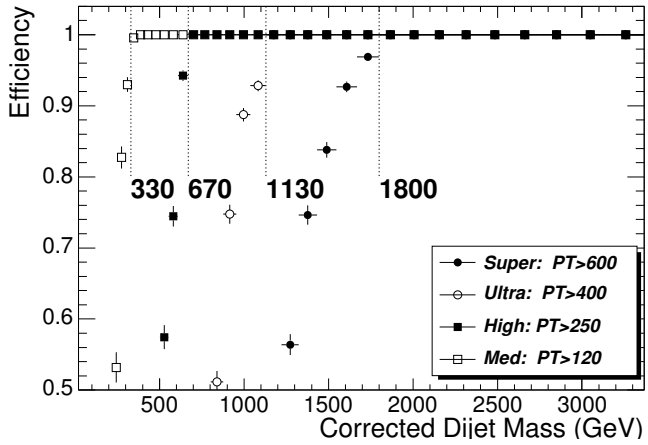

Figure 7.4: Jet trigger efficiency (points) and fully efficient dijet mass cuts (lines).

will use to measure the cross section. We use each trigger where it is fully efficient and stop

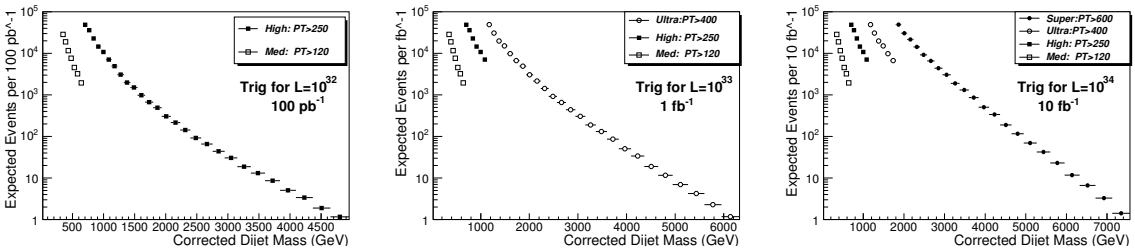

Figure 7.5: Rate of jet trigger for cross section measurement. Same triggers as Fig. 7.3.

using the trigger where the next trigger is fully efficient. Fig. 7.5 shows there are adequate

numbers of fully efficient events for analysis.

7.3.4 Dijet Mass Distribution from QCD

In Fig. 7.6 we combine the triggers to produce a cross section across the full mass spectrum. The prescaled triggers allow us to measure mass down to 300 GeV, or even smaller if we

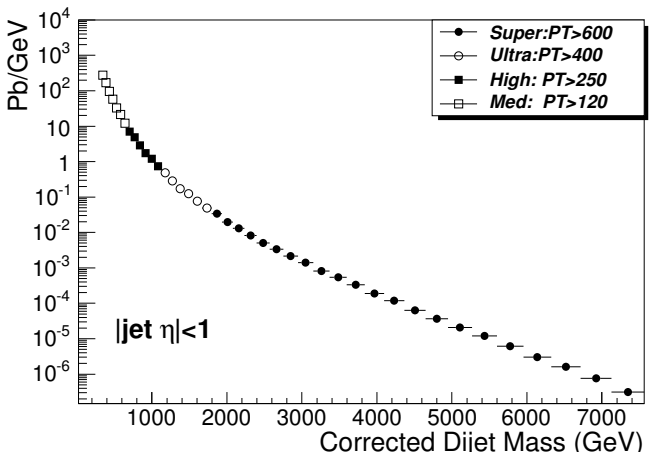

Figure 7.6: Cross section vs. dijet mass and the contributing jet triggers.

can understand the efficiency of the lowest threshold trigger. The mass measured with the prescaled triggers will allow us to connect to dijet masses measured at the Tevatron.

In Fig. 7.7 we show the fractional statistical error on the cross section, the simplest measure of our sensitivity to new physics. Fig. 7.7 shows that our prescaled triggers will allow a

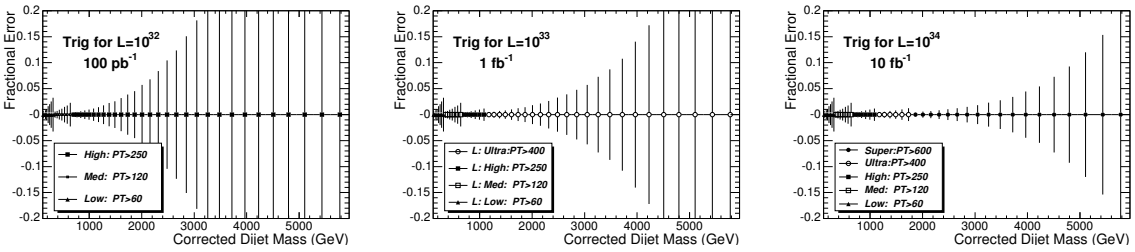

Figure 7.7: Fractional statistical error on the jet cross section for the samples in Fig. 7.7.

measurement of QCD with 1-3% statistical accuracy. The unprescaled triggers will have 1% error at threshold and the first unprescaled sample begins at a mass of 670 GeV, giving us full sensitivity to new physics in a region that overlaps with previous dijet mass measurements at the Tevatron.

7.3.5 Searches using Dijet Mass

Here we will discuss the signal and background distributions that are needed for a dijet resonance search using the mass distribution. In section 17.4.2 we use these techniques to estimate our sensitivity to seven models of narrow dijet resonances.

7.3.5.1 Narrow Dijet Resonance Shapes

The simulated shape of a narrow dijet resonance in CMS is shown in Figure 7.8. The shape is composed of a Gaussian distribution from jet energy resolution and a long tail to low mass. The measured RMS of the Gaussian component is $\sigma/M = 0.045 + 1.3/\sqrt{M}$. The long tail to low mass comes predominately from final state QCD radiation (extra jets) which reduce the reconstructed mass. All resonances with a natural width significantly less than our resolution should look similar to this in the CMS detector. The model used in Figure 7.8 was a Z' from Pythia.

7.3.5.2 QCD Background to Dijet Resonances

Figure 7.8 compares a Z' signal cross section to the QCD background found in section 7.3.4. The differential cross section for the QCD background is well fit by a simple parameterization

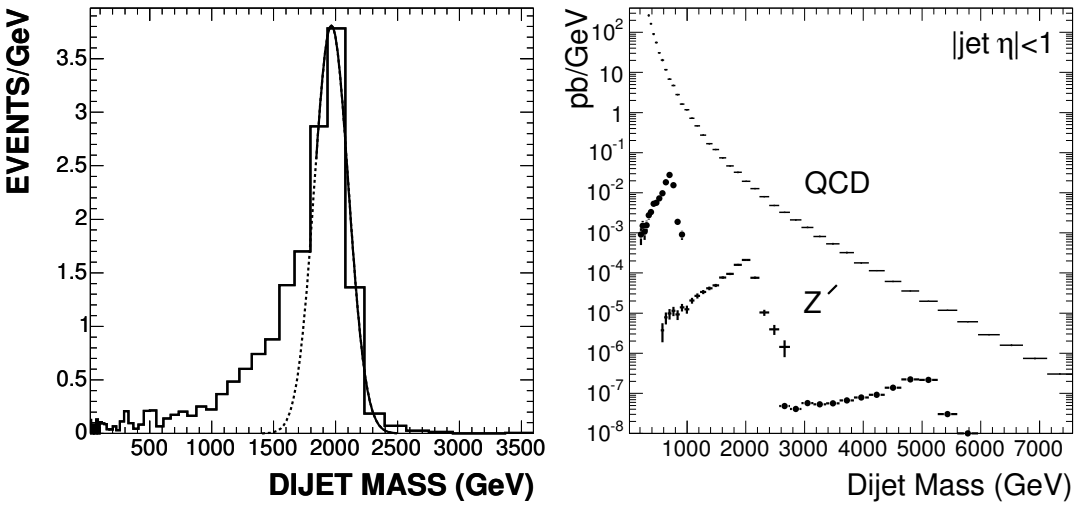

Figure 7.8: Left) The dijet mass distribution from a 2 TeV/c^2 Z' (histogram) is fit with a Gaussian (solid curve) from the peak region to high mass and the Gaussian is extended to lower mass (dashed curve). Right) The differential cross section as a function of dijet mass for the QCD background and three Z' signals with a mass of 0.7, 2, and 5 TeV/c^2.

of the form

$$\frac{d\sigma}{dm} = \frac{p_0(1 - m/\sqrt{s})^{p_1}}{m^{p_2}} \tag{7.1}$$

where m is the dijet mass, $\sqrt{s} = 14000$ GeV/c^2 is the collision energy, and p_0, p_1, p_2 are arbitrary parameters. The resonance sensitivity estimates in section 17.4.2 use this parameterization to smooth away background fluctuations in our simulation sample. In a search with real data, a similar parameterization could be used to simply model the measured background, as was done by CDF [4], or a full NLO QCD calculation smeared with the jet resolution could be used to model the background, as was done by D0 [5].

7.3.6 Searches using Dijet Mass and Angle

Here we will discuss the signal and background distributions that are used for searches for new physics in the dijet mass and angular distribution simultaneously. This technique can be used to confirm resonances observed in the dijet mass distribution, and measure their spin, or to discover other new physics that could affect the dijet angular distribution. In section 17.4.3 we use these techniques to estimate our sensitivity to a model of quark contact interactions.

7.3.6.1 Dijet Ratio: $N(|\eta| < 0.5)/N(0.5 < |\eta| < 1.0)$

The ratio of the number of dijets in which both jets have $|\eta| < 0.5$ to the number of dijets in which both jets have $0.5 < |\eta| < 1.0$ was first introduced by D0 to search for contact interactions as a function of dijet mass [6]. It is the simplest measure of the most sensitive part of the angular distribution, providing a single number we can measure as a function of dijet mass. In Figure 7.9 we show our lowest order calculation of the dijet ratio from QCD compared with a left-handed contact interaction among quarks [7, 8] at three different values of the contact interaction scale. For this calculation we used the same code as [9] with modern parton distributions [10]. Lowest order QCD gives a fairly flat dijet ratio around 0.6

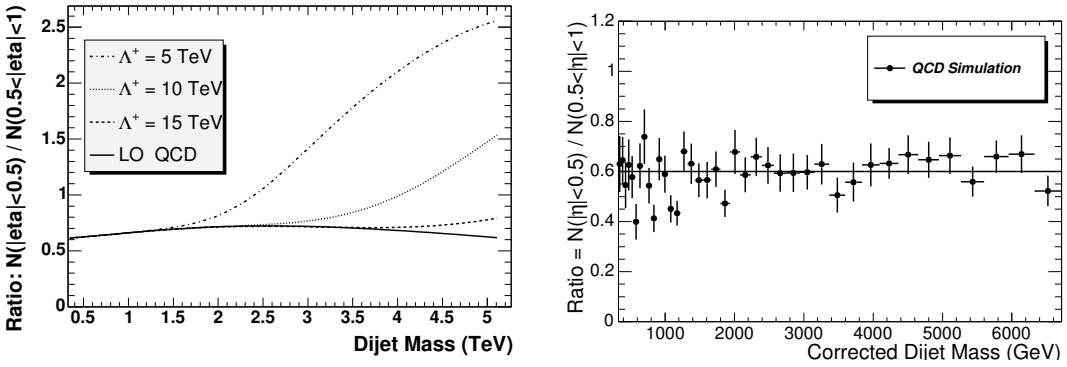

Figure 7.9: Left) A lowest order calculation of the dijet ratio from QCD (solid curve) is compared with QCD plus a quark contact interaction at a scale Λ^+ of 15 TeV (dashed), 10 TeV (dotted) and 5 TeV (dot-dashed). Right) The dijet ratio in the CMS simulation from QCD (points) is compared to the value 0.6 (line).

while the contact interactions produce an increase in the dijet ratio at high mass. Figure 7.9 also shows that a full CMS detector simulation of the dijet ratio from QCD, using the samples discussed in section 7.3.4, is indistinguishable from a flat ratio of 0.6 within the simulation statistical uncertainty.

7.3.7 Systematic Uncertainties

In figure 7.10 we present estimates of systematic uncertainties on both the dijet cross section and the dijet ratio. The systematics discussed below have a large affect on the cross section and little affect on the dijet ratio.

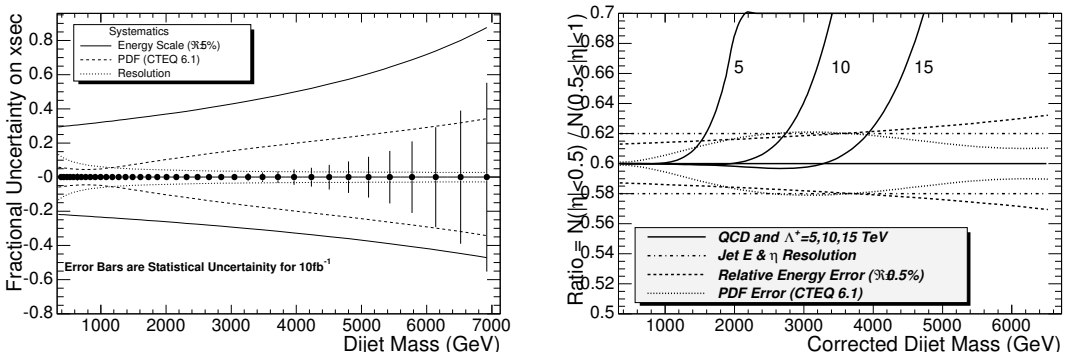

Figure 7.10: Left) Systematic uncertainty on the dijet cross section due to jet energy scale (solid curve), parton distributions (dashed curve), and calorimeter energy and η resolution (dotted curve) are compared to the statistical uncertainties for 10 fb^{-1}(error bars). Right) Systematic bounds on the dijet ratio from uncertainties in the relative jet energy scale (dashed curve), parton distributions (dotted curve), and calorimeter energy and eta resolution (dot dash curve), are compared to the expectations of QCD and three contact interaction scales (solid line and curves).

7.3.7.1 Absolute Jet Energy Scale

We have concluded that an overall uncertainty on the jet energy scale in the barrel of $\pm 5\%$ is achievable [11]. We have propogated this energy scale error to the dijet mass cross section by measuring the effect of a $\pm 5\%$ change in mass on a smooth fit to the dijet mass cross section. As shown in figure 7.10, the resulting upper uncertainty on the cross section varies from 30% at a dijet mass of 0.3 TeV/c^2 to 80% at a dijet mass of 6.5 TeV. This large systematic uncertainty, increasing with dijet mass, is the primary reason we do not use the dijet mass distribution to search for quark contact interactions. For the dijet ratio the absolute jet energy scale uncertainty has no effect, because the dijet ratio is flat versus dijet mass. The uncertainty cancels out in the ratio.

7.3.7.2 Relative Jet Energy Scale

We have shown that by using dijet balance an uncertainty of $\pm 0.5\%$ is achievable [12] for the relative jet energy scale as a function of η within the barrel, in 0.1 steps in η. Here we assume that the relative jet energy scale, defined in this analysis as the uniformity in energy scale in the region $0.5 < |\eta| < 1.0$ compared to $|\eta| < 0.5$, can be determined to $\pm 0.5\%$. For the cross section as a function of mass this uncertainty is negligible compare to the $\pm 5\%$ error in the absolute energy scale. We have propagated this error to the dijet ratio by measuring the effect of a $\pm 0.5\%$ change in dijet mass for the measurement of $N(0.5 < |\eta| < 1)$ while keeping $N(|\eta| < 0.5)$ unchanged. As shown in figure 7.10, the resulting upper uncertainty in the ratio varies from 0.013 (2%) at a mass of 0.3 TeV/c^2 to 0.032 (5%) at a mass of 6.5 TeV.

7.3.7.3 Resolution

The effect of calorimeter resolution is the difference between the measurement with jets constructed from MC particles (Gen Jets) and the measurement with jets constructed from calorimeter depositions and corrected (Rec Jets). This difference, often called the smearing

due to calorimeter resolution, is taken as a bound on the size of the systematic uncertainty due to resolution. For the cross section, the difference between Rec Jets and Gen Jets is small. This smearing varies from 15% at 0.3 TeV to 3% at 6.5 TeV, as shown in Figure 7.10. For the ratio, there is no change between Gen Jets and corrected Rec Jets within the Monte Carlo statistics presented in Fig. 7.9, and the statistical error on the simulation gives a bound on the systematic of 0.02 (3%) in the ratio, which is shown in Figure 7.10.

7.3.7.4 Parton Distributions

CTEQ 6.1 provides parton distributions with systematic uncertainties coming from the world data on parton distribution functions (PDFs) and the fit to world data [10]. CTEQ 6.1 has 40 different error PDFs, 20 PDFs at positive error, and 20 PDFs at negative error. We have used these 40 PDFs and the recommended procedure [10] to calculate the PDF uncertainties on both the cross section and the dijet ratio using our lowest order QCD calculation. As shown in figure 7.10, the resulting upper uncertainty in the cross section varies from 5% at a dijet mass of 0.3 TeV to 32% at a dijet mass of 6.5 TeV. As shown in figure 7.10, the resulting uncertainty in the dijet ratio peaks at a value of 0.02 (3%) in the ratio at a mass of around 3.5 Tev, and declines at both lower and higher masses.

7.3.7.5 Luminosity, Efficiency and Acceptance

The luminosity uncertainty on the cross section is around 10%, small compared to other uncertainties, and has no affect on the dijet ratio. For the masses we consider in this analysis there is full efficiency for finding a dijet in the event with negligible uncertainty. The acceptance for jets is defined by the cut in η, and any measured jet distributions must be compared to calculations using the same η cuts, with negligible uncertainty in the comparison of measured and calculated jet η.